

Motion Tracking of the Carotid Artery Wall from Ultrasound Image Sequences: a Nonlinear State-space Approach

Zhifan Gao, Yanjie Li, Yuanyuan Sun, Jiayuan Yang, Huahua Xiong, Heye Zhang, *Member, IEEE*, Xin Liu, Wanqing Wu, Dong Liang, and Shuo Li

Abstract—The motion of the common carotid artery (CCA) wall has been established to be useful in early diagnosis of atherosclerotic disease. However, tracking the CCA wall motion from ultrasound images remains a challenging task. In this study, a nonlinear state-space approach has been developed to track CCA wall motion from ultrasound sequences. In this approach, a nonlinear state-space equation with a time-variant control signal was constructed from a mathematical model of the dynamics of the CCA wall. Then, the unscented Kalman filter (UKF) was adopted to solve the nonlinear state transfer function in order to evolve the state of the target tissue, which involves estimation of the motion trajectory of the CCA wall from noisy ultrasound images. The performance of this approach has been validated on 30 simulated ultrasound sequences and a real ultrasound dataset of 103 subjects by comparing the motion tracking results obtained in this study to those of three state-of-the-art methods and of the manual tracing method performed by two experienced ultrasound physicians. The experimental results demonstrated that the proposed approach is highly correlated with (intra-class correlation coefficient ≥ 0.9948 for the longitudinal motion and ≥ 0.9966 for the radial motion) and well agrees (the 95% confidence interval width is 0.8871 mm for the longitudinal motion and 0.4159 mm for the radial motion) with the manual tracing method on real data and also exhibits high accuracy on simulated data (0.1161 ~ 0.1260 mm). These results appear to demonstrate the effectiveness of the proposed approach for motion tracking of the CCA wall.

Index Terms—Vessel wall motion, carotid ultrasound, unscented Kalman filter, block matching method, atherosclerosis

I. INTRODUCTION

EARLY diagnosis is a key component for prevention of mortality and morbidity from atherosclerotic diseases.

The work was supported by the National Key Research and Development Program of China (2016YFC1301702, 2016YFC1300302), National Natural Science Foundation of China (No. 61771464), the Science Technology and Innovation Committee of Shenzhen for Research Projects (JCYJ20151030151431727, SGLH20150213143207911, SGLH20150216172854731, JCYJ20170307165309009), the National High Technology Research and Development Program (863 Program, SS2015AA020109), and the CAS Presidents International Fellowship for Visiting Scientists (2017VTA0011). (*Corresponding authors: Heye Zhang*)

Z. Gao, H. Zhang, X. Liu, W. Wu and D. Liang are with Shenzhen Institutes of Advanced Technology, Chinese Academy of Sciences, Shenzhen, 518055, China (email: {zf.gao, hy.zhang, liu.xin, wq.wu, dong.liang}@siat.ac.cn).

Y. Li, Y. Sun and J. Yang are with Harbin Institute of Technology Shenzhen Graduate School, Shenzhen, 518055, China (email: lyj@hitsz.edu.cn).

H. Xiong is with Department of Ultrasound, the Second People's Hospital of Shenzhen, Shenzhen, 518035, China.

S. Li is with University of Western Ontario, London, N6A 3K7, Canada (email: slishuo@gmail.com).

Although both the processes of arterial stiffening and thickening originate from the dysregulation of the balance between the components of collagen and elastin in the artery wall, arterial stiffening generally occurs before arterial thickening in the atherosclerosis progression [1]. Therefore, attempts have been made to quantify carotid arterial stiffness in order to determine the degree of atherosclerotic disease for early diagnosis [2]. As carotid ultrasound is a relatively inexpensive, radiation-free, and noninvasive imaging modality, the analysis of common carotid artery (CCA) wall motion (radial & longitudinal motion) using an ultrasound sequence for determining the degree of arterial stiffness is an effective approach while conducting screening tests for atherosclerotic disease among members of a large population [3]. Furthermore, CCA wall motion has been recently considered as an independent predictor of atherosclerotic disease [4]. Nevertheless, the delineation of motion trajectories of the CCA wall continues to be challenging for medical physicians as it is a laborious and time-consuming task. Therefore, the development of a computer-aided approach to track the CCA wall motion is in high demand.

In response, several studies have developed computer-aided methods to reliably and efficiently track CCA wall motion in ultrasound imaging sequences. In general, these studies applied a model-free method or a model-based method to perform the motion-tracking task. Model-free methods estimate the dynamics of the target object by using information on local image structures without considering prior information or model assumption regarding these structures. The block matching (BM) method is a widely used model-free method [5] and has been applied in the tracking of CCA wall motion in recent years [6], [7]. However, model-free methods are adversely affected by the instability of the local image structures. This instability originates from three aspects: the low intensity contrast owing to the homogeneity of the tissue texture in the longitudinal direction of the CCA wall; loss of image detail from the relatively low-resolution ultrasound image owing to the shape of the scanner's point spread function; and variation of the local image structure owing to the image noise, out-of-plane motion, and tissue deformation of the CCA wall. In the BM method, this instability is likely to progressively bias the best-matched block to the template of the target tissue during the motion tracking process. This is because the similarity criterion used in the BM method is based on the local intensity diversity of the search region [8].

In order to overcome disadvantages of model-free methods, model-based methods apply extra models to constrain the dynamics of the CCA wall and thus enhance the resistance to the effect of instability from the local image structures. One of these methods use a forward model described by the state-space equation (see equation 1) to estimate the state (such as appearance and location) of the reference block in successive frames. This model gathers information from observations of the reference block under the assumption that the state variation is a Markov process. The most common of such methods is Kalman filter. The Kalman filter provides a best-linear-unbiased estimator based on the minimum-mean-square-error sense or the L_2 sense. One of the first such studies applied the Kalman filter in the tracking of CCA wall motion to evolve the state of the block using observation information obtained by the BM method [9]. Two other combinations of the Kalman filter and BM method were subsequently developed for refining the motion trajectories of the CCA wall [10]. One of the combined methods applied the Kalman filter to correct the location of the best-matched block in a frame immediately following the block computation. The other method used the Kalman filter to correct the motion trajectories while all the frames were processed by the BM method. [10] also demonstrated that the tracking performance of CCA wall motion can be improved by updating either the appearance or the position of the reference block in the Kalman-based method. More recently, a study introduced a more robust Kalman-based method [11]. This promising work first applied a control signal to the state-space equation (which corresponds to the gray-level appearance in the first frame of the sequence) to reduce the bias of the motion trajectory toward the quasi-periodic real motion. [12] compared the BM and Kalman-based methods in the tracking of CCA wall motion. These Kalman-based block matching methods, however, consider the motion of the target tissue on the CCA wall as a linear dynamic process. This linear assumption of the dynamic process is likely to have contributed to the deviation between the estimated motion and real motion because of the potential nonlinear dynamics in CCA wall motion.

In this study, a nonlinear state-space approach was developed to track CCA wall motion. The Markovian state-space approach also considers the information on earlier CCA wall motion. This can overlook significant displacement in the target block in successive frames and addressing the instability of the local image structures. In order to effectively address the nonlinear components of this motion, we proposed a nonlinear quasi-periodic function to match the dynamics of the CCA wall in the state-space equations [13] and estimated the state variation of the target tissue by using the unscented Kalman filter (UKF) on the observations from the BM method. In addition, we applied a time-variant control signal from a mathematic model [14], [15], to correct the biased displacements of the block during the motion tracking process. The performance of this approach was tested on a set of monitored ultrasound imaging sequences acquired from 103 subjects, and was compared to the manually traced results by two ultrasound physicians and three state-of-the-art methods.

II. METHODOLOGY

The proposed approach tracks CCA wall motion. The nonlinear component of carotid dynamics was approximated by setting the state transfer function in the state-space equation to be a nonlinear quasi-periodic function (Section II-A) [13]. Moreover, the estimation of the motion trajectories was corrected by considering a mathematical model of CCA wall motion as the control signal of the state-space equations [14]. This enhances the resistance to disturbance from uncertainty in ultrasound imaging. Then, for appropriately approximating the nonlinear quasi-periodic function and reliably updating the state with time, the UKF was adopted to solve the state-space equation (Section II-B and II-C).

A. Model Description

The dynamics of the CCA wall is assumed to satisfy the state-space equations:

$$\mathbf{x}_{n+1} = f(\mathbf{x}_n, \mathbf{u}_n) + \mathbf{w}_n, \quad \mathbf{y}_n = h(\mathbf{x}_n) + \mathbf{v}_n \quad (1)$$

where n is the frame index, \mathbf{x}_n is the state of the target tissue evolved by the UKF, and \mathbf{y}_n is the observation of the target tissue updated by the BM method. \mathbf{w}_n and \mathbf{v}_n are independent noise terms that obey the Gaussian distribution, i.e. $\mathbf{w}_n \sim \mathcal{N}(0, \mathbf{Q})$ and $\mathbf{v}_n \sim \mathcal{N}(0, \mathbf{R})$. \mathbf{Q} and \mathbf{R} are the covariance matrices of noise and set to $q\mathbf{I}$ and $r\mathbf{I}$. The state \mathbf{x}_n of the target tissue is defined as the location of the center point of the reference block $\mathbf{B}_n^{\text{ref}}$ ($x_n = [x_n^1, x_n^2]^T$, where x_n^1 is the x-coordinate of the center point and x_n^2 is the y-coordinate). The state function f is motivated by the Van der Pol oscillator [13] and is formulated as

$$\begin{aligned} x_{n+1}^1 &= x_n^1 - \frac{T}{5}x_n^2 + Tu_1 \\ x_{n+1}^2 &= \left(1 - \frac{T}{5}\right)x_n^2 + Tx_n^1 - \frac{T}{373}x_n^1x_n^2 + Tu_2 \end{aligned} \quad (2)$$

where T is the sampling period, i.e. the number of ultrasound frames sampled in a cardiac cycle. The control signal $\mathbf{u}_n = [u_1, u_2]^T$ is motivated by a mathematical model of mechanical deformation of the CCA wall [14], [15] formulated by $\mathbf{u}_n = \mathbf{g}_1(n) + \mathbf{g}_2(n)$, where $\mathbf{g}_1(n)$ and $\mathbf{g}_2(n)$ are expressed as follows:

$$\begin{aligned} \mathbf{g}_1(n) &= \frac{1}{4} \begin{bmatrix} \tanh(1.22(n - 0.4T))(1 - \tanh(1.22n)) \sin^2 \frac{\pi n}{3.5T} \\ \tanh(2.07(n - 0.4T))(1 - \tanh(2.07n)) \sin^2 \frac{\pi n}{3.5T} \end{bmatrix} \\ \mathbf{g}_2(n) &= \frac{1}{4} \begin{bmatrix} (1 + \tanh(1.22(n - T)))(1 + \tanh(1.22(0.4T - n))) (20 - \frac{20}{T}n) \\ (1 + \tanh(2.07(n - T)))(1 + \tanh(2.07(0.4T - n))) (17 - \frac{17}{T}n) \end{bmatrix} \end{aligned} \quad (3)$$

The solution of the state-space equations in equation (1) aims to obtain the optimum estimate $\hat{\mathbf{x}}_n$ of the state \mathbf{x}_n . This best estimate is computed by using the UKF. This filter aims to approximate the nonlinear transformation (the function f in equation 1) by evolving a set of points (sigma points) that are sampled around their mean value. It is capable of decreasing the error from the linearized transformation of the non-linear function.

B. State Prediction

In the state prediction step, the state \mathbf{x}_n in equation (1) is estimated by the UKF. The UKF aims to evolve the state of the non-linear state-space equations and approximate the non-linear state transfer function based on the unscented transformation [16]. Before the motion tracking (in the state-space approach), three reference blocks in the first frame of each sequence in our ultrasound data are specified by experts (see Figure 1(a)). The three reference blocks are then tracked independently in the subsequent frames. For the UKF process, the initial state \mathbf{x}_0 is the location of one of the three user-specified reference blocks, and the corresponding initial auto-covariance (denoted by \mathbf{P}_0 or $(\mathbf{P}_0^{xx})^+$) is the parameter determined in Section III-C. The complete UKF algorithm can be summarized as follows:

Assume that the sigma points $\hat{\mathbf{x}}_{n-1}^s$ in the $n-1$ th ultrasound frame are known. The sigma points $\tilde{\mathbf{x}}_n^s$ in the n th frame can be obtained by appropriately modifying $\hat{\mathbf{x}}_{n-1}^s$ by the non-linear function f in equation (1):

$$\tilde{\mathbf{x}}_n^s = f(\hat{\mathbf{x}}_{n-1}^s, \mathbf{u}_{n-1}) \quad (4)$$

The superscript s denotes the s th sigma point. The priori estimation of state $\hat{\mathbf{x}}_n^-$ and auto-covariance of the observation $(\mathbf{P}_n^{xx})^-$ can be estimated by the following equations:

$$\begin{aligned} \hat{\mathbf{x}}_n^- &= \sum_{s=1}^{2M} \alpha^s \tilde{\mathbf{x}}_n^s \\ (\mathbf{P}_n^{xx})^- &= \sum_{s=1}^{2M} \beta^s (\tilde{\mathbf{x}}_n^s - \hat{\mathbf{x}}_n^-) (\tilde{\mathbf{x}}_n^s - \hat{\mathbf{x}}_n^-)^T + \mathbf{Q} \end{aligned} \quad (5)$$

where $2M$ is the number of sigma points, α^s is the weight for the mean related to the s th sigma point, and β^s is the weight for the covariance related to the s th sigma point. The formulation of $\hat{\mathbf{x}}_n^s$, α^s and β^s are obtained by the unscented transformation in Section II-C.

Then, the observation equation is used in equation (1) to transform the sigma points $\hat{\mathbf{x}}_n^s$ of the state into the sigma points $\hat{\mathbf{y}}_n^s$ of the observation; moreover, observation $\hat{\mathbf{y}}_n$ is estimated as follows:

$$\hat{\mathbf{y}}_n^s = h(\hat{\mathbf{x}}_n^s), \quad \hat{\mathbf{y}}_n = \sum_{s=1}^{2M} \alpha^s \hat{\mathbf{y}}_n^s \quad (6)$$

By the estimation of the state, the observation $\hat{\mathbf{x}}_n^-$ and $\hat{\mathbf{y}}_n$, and their sigma points $\hat{\mathbf{x}}_n^s$ and $\hat{\mathbf{y}}_n^s$, the auto-covariance of the observation \mathbf{P}_n^{yy} and cross covariance of the state and the observation \mathbf{P}_n^{xy} can be obtained as:

$$\begin{aligned} \mathbf{P}_n^{yy} &= \sum_{s=1}^{2M} \beta^s (\hat{\mathbf{y}}_n^s - \hat{\mathbf{y}}_n) (\hat{\mathbf{y}}_n^s - \hat{\mathbf{y}}_n)^T + \mathbf{R} \\ \mathbf{P}_n^{xy} &= \sum_{s=1}^{2M} \beta^s (\tilde{\mathbf{x}}_n^s - \hat{\mathbf{x}}_n^-) (\hat{\mathbf{y}}_n^s - \hat{\mathbf{y}}_n)^T \end{aligned} \quad (7)$$

The Kalman gain can be computed using \mathbf{P}_n^{xy} and \mathbf{P}_n^{yy} as

$$\mathbf{K}_n = \mathbf{P}_n^{xy} (\mathbf{P}_n^{yy})^{-1} \quad (8)$$

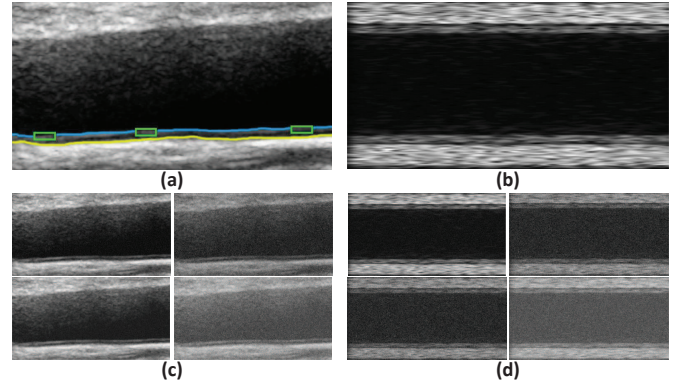


Fig. 1. (a) Sample real carotid ultrasound image. The blue curve and yellow curve are the lumen border and media-adventitia border, respectively, of the carotid artery. (b) Sample synthetic carotid ultrasound image. (c) Real carotid ultrasound images corrupted by Rayleigh (first row) and Gaussian (second row) noise with 16dB (first column) and 2dB (second column) SNR. (d) Synthetic carotid ultrasound images corrupted by Rayleigh (first row) and Gaussian (second row) noise with 16dB (first column) and 2dB (second column) SNR.

The posteriori estimation of state $\hat{\mathbf{x}}_n^+$ and auto-covariance of the state $(\mathbf{P}_n^{xx})^+$ can be obtained using

$$\begin{aligned} (\mathbf{P}_n^{xx})^+ &= (\mathbf{P}_n^{xx})^- - \mathbf{K}_n \mathbf{P}_n^{yy} \mathbf{K}_n^T \\ \hat{\mathbf{x}}_n^+ &= \hat{\mathbf{x}}_n^- + \mathbf{K}_n (\mathbf{y}_n - \hat{\mathbf{y}}_n) \end{aligned} \quad (9)$$

where \mathbf{y}_n is the observation of the target block in the n th ultrasound frame. The best-matched block is computed by determining the candidate block most similar to the reference block in the block matching method [7]. In the experiments, we tested three commonly used block matching criteria [5]: mean absolute difference, mean square error and normalized cross correlation. Their comparison is presented in Section III-C.

Finally, the sigma points $\hat{\mathbf{x}}_n^s$ is updated for the state prediction in the subsequent frame:

$$\hat{\mathbf{x}}_n^s = \hat{\mathbf{x}}_n^+ + \check{\mathbf{x}}_n^s \quad (10)$$

where $\check{\mathbf{x}}_n^s$ are the points in the vicinity of the posteriori state estimate $\hat{\mathbf{x}}_n^+$ in the state space, and its computation is presented in Section II-C.

C. The unscented transformation

In the process of solving the nonlinear state-space system, it is difficult to transform a probability density function through a general nonlinear function. The unscented transformation provides an approach to use the exact nonlinear function to approximate such a probability distribution [17]. Three commonly used unscented transformations have been used in this study and the optimum one was selected (see Section III-C). The main dissimilarity among the three types of unscented transformations is the dissimilarity in their ability to compute the sigma points based on the neighborhoods with various structures. The selected unscented transformation is then used to compute $\hat{\mathbf{x}}_{n-1}^s$ in equation (10), and α^s , β^s in equation (5) of the UKF process (see Section II-B):

Unscented transformation 1 [17]:

$$\tilde{\mathbf{x}}_{n-1}^s = \begin{cases} \left(\sqrt{M(\mathbf{P}_{n-1}^{xx})^+} \right)^T, & s = 1, 2, \dots, M \\ - \left(\sqrt{M(\mathbf{P}_{n-1}^{xx})^+} \right)^T, & s = M + 1, \dots, 2M \end{cases} \quad (11)$$

where the subscript s is the s th row of the matrix $(\sqrt{M(\mathbf{P}_{n-1}^{xx})^+})^T$. The weights α^s and β^s are defined by

$$\alpha^s = \beta^s = \frac{1}{2M}, \quad s = 1, 2, \dots, 2M \quad (12)$$

Unscented transformation 2(Scaled unscented transformation) [18]:

$$\tilde{\mathbf{x}}_{n-1}^s = \begin{cases} 0, & s = 0 \\ \left(\sqrt{(M + \lambda)(\mathbf{P}_{n-1}^{xx})^+} \right)^T, & s = 1, 2, \dots, M \\ - \left(\sqrt{(M + \lambda)(\mathbf{P}_{n-1}^{xx})^+} \right)^T, & s = M + 1, \dots, 2M \end{cases} \quad (13)$$

where $\lambda = (\epsilon^2 - 1)M$ is a scaling parameter, and ϵ is a marginal constant. The subscript s denotes the s th row of the matrix $(\sqrt{(M + \lambda)(\mathbf{P}_{n-1}^{xx})^+})^T$. The weights α^s and β^s are defined by

$$\begin{aligned} \alpha^0 &= \frac{\lambda}{M + \lambda}, \quad \beta^0 = \frac{\lambda}{M + \lambda} + (1 - \epsilon^2 + \gamma) \\ \alpha^s &= \beta^s = \frac{1}{2(M + \lambda)}, \quad s = 1, 2, \dots, 2M \end{aligned} \quad (14)$$

where γ contains the prior knowledge of the distribution of the state. In this approach, $\epsilon = 0.001$ and $\gamma = 2$.

Unscented transformation 3(Symmetric unscented transformation) [19]:

$$\tilde{\mathbf{x}}_{n-1}^s = \begin{cases} 0, & s = 0 \\ \left(\sqrt{(M + \sigma)(\mathbf{P}_{n-1}^{xx})^+} \right)^T, & s = 1, 2, \dots, M \\ - \left(\sqrt{(M + \sigma)(\mathbf{P}_{n-1}^{xx})^+} \right)^T, & s = M + 1, \dots, 2M \end{cases} \quad (15)$$

where the weights α^s and β^s are defined by

$$\begin{aligned} \alpha^0 &= \beta^0 = \frac{\sigma}{M + \sigma} \\ \alpha^s &= \beta^s = \frac{1}{2(M + \sigma)}, \quad s = 1, 2, \dots, 2M \end{aligned} \quad (16)$$

where σ is a parameter set to be 1 in this approach.

III. EXPERIMENTS

A. Data Collection

The proposed approach was tested on both real image data and synthetic image data. The real image data were collected by an experienced ultrasound physician using a high-resolution ultrasound system (iU22 Philips Ultrasound, Bothell, WA, USA) and a 7.5MHz linear array transducer. A total of 22 healthy subjects (15 males, 53.07 ± 10.48 age years; 7 females,

TABLE I
COMPARISON OF THREE UNSCENTED TRANSFORMATIONS UT_{scal} , UT_{sym} , AND UT_{2n} . THE SIGNIFICANCE TESTS REVEAL THAT THE TRACKING ERRORS (MEASURED BY w_l , w_r AND w_t IN MILLIMETERS) OF OUR APPROACH USING UT_{2n} HAVE SIGNIFICANT DIFFERENCE FROM THAT USING UT_{scal} AND UT_{sym} (THE SIGNIFICANCE LEVEL IS 0.05).

Method	w_l	w_r	w_t
UT_{scal}	0.1935 (± 0.0809)	0.1157 (± 0.0370)	0.2296 (± 0.0761)
UT_{sym}	0.1934 (± 0.0812)	0.1157 (± 0.0371)	0.2295 (± 0.0764)
UT_{2n}	0.1933 (± 0.0807)	0.1156 (± 0.0370)	0.2293 (± 0.0759)
P-value	w_l	w_r	w_t
UT_{2n} vs UT_{scal}	<0.01	<0.01	<0.01
UT_{2n} vs UT_{sym}	<0.01	<0.01	0.2732

57.71 ± 8.83 age years) and 81 patients (49 males, 57.87 ± 12.71 age years; 32 females, 60.40 ± 12.07 age years) were included in the real image data. The patients were diagnosed to be suffering from one of three diseases: heart disease (cardiovascular disease due to atherosclerosis [20]), type 1 or 2 diabetes (fasting blood glucose ≥ 126 mg/dl) and hypertension (systolic blood pressure ≥ 140 mmHg or diastolic blood pressure ≥ 90 mmHg). Each participant was informed of the purpose and procedure of this study. Informed consent was obtained from each participant. This study was approved by the Second People's Hospital of Shenzhen (China), and followed the Declaration of Helsinki (2013). All the real image data were saved in Digital Imaging and Communications in Medicine (DICOM) format into CDs for off-line analysis. During data collection, subjects were examined in the supine position, with the head turned 45° away from the examined side. The following settings of the ultrasound machine were used for all acquisitions: dynamic range was 60 dB, sequence frame rate was 24-51 frames/second, pixel size in both radial and longitudinal directions was 19.2 pixels/mm. Figure 1(a) illustrated a sample of the read image, and Figure 1(c) shows the corresponding noise-corrupted images.

The synthetic image data were simulated using an ultrasound simulation system (Field II) [21]. Firstly, ten phantoms similar to the anatomic structure of the carotid artery were generated. Then, three ultrasound sequences were generated from each of these phantoms (totally 30 sequences) separately in 5 MHz, 7.5 MHz, and 10 MHz central frequencies; these simulated carotid arteries were then made to move in the trajectory of the sine wave along both the radial (amplitude: 0.5 mm; frequency 1.5 Hz) and longitudinal directions (amplitude: 0.3 mm; frequency 1.0 Hz). Other transducer parameters included a 64-element linear array with Hanning apodization for both transmission and reception. The sampling frequency of the scanning was 100 MHz. In addition, different levels (2dB~30dB signal-noise ratio) of Rayleigh noise and Gaussian noise were artificially added to the synthetic image data. Figure 1(b) illustrates a sample of the synthetic image, and Figure 1(d) illustrates the corresponding noise-corrupted images.

B. Performance Evaluation

The CCA wall motion in an ultrasound sequence was measured by the longitudinal position (LP) and radial position

(RP) of the block in every ultrasound frame. The performance was evaluated by comparing LP and RP values between our approach and the manual tracing method (performed by two experienced ultrasound physicians). This evaluation was analyzed based on three aspects: correlation, agreement, and error.

Considering the potential influence of multiple measurement of each subject and between-subject variation on the performance of our approach, the subjects in this study were divided into groups by sex (male and female), health condition (healthy and unhealthy), and age (40-49 years old; 50-59 years old; 60-69 years old; 70-79 years old); then, the correlation from the linear mixed-effects model with two levels [22] were investigated. Level-1 explanatory variable (denoted by \mathcal{X}) is the multiple measurement of LP or RP in each subject computed only by our approach. Level-2 explanatory variables include health condition, age, and sex. The dependent variable (denoted by \mathcal{Y}) is the manual tracing result corresponding to the Level-1 explanatory variable. This linear mixed-effects model can be formulated as

$$\begin{aligned} \mathcal{Y} = & \beta_0 + \beta_1\mathcal{X} + \beta_2\text{Health} + \beta_3\text{Sex} + \beta_4\text{Age} \\ & + \beta_5\mathcal{X} * \text{Health} + \beta_6\mathcal{X} * \text{Sex} + \beta_7\mathcal{X} * \text{Age} \quad (17) \\ & + u_0 + u_1\mathcal{X} + \varepsilon \end{aligned}$$

$\beta_0 - \beta_7$, u_0 and u_1 are parameters of the above linear mixed-effects model. β_0 is the intercept. $\beta_1 - \beta_7$ are fixed effects. $\mathcal{X} * \text{Health}$, $\mathcal{X} * \text{Sex}$, and $\mathcal{X} * \text{Age}$ reveal the across-level interactions. u_0 and u_1 are the random effects. ε is the residual. The statistical significance with the null hypothesis that these parameters equal zero provides the effects of the explanatory variables on the dependent variable. The significance level is 0.05.

Then, the agreement between our approach and the manual traced method was investigated by two commonly used evaluation methods: intraclass correlation coefficient (ICC) and Bland-Altman analysis. The ICC for two-way model was computed in terms of absolute agreement (denoted by ICC(A,1)) and consistency (denoted by ICC(C,1)) [23]. For Bland-Altman analysis, the plot of the differences between our approach and the manual traced method were produced against their averages to demonstrate the agreement [24].

The performance of our approach was measured by calculating the tracking errors of the longitudinal motion trajectory w_l , radial motion trajectory w_r , and 2D motion w_t , between our approach and the manual tracing method. These three errors are defined as [9]:

$$\begin{aligned} w_l &= \sqrt{\frac{\sum_{i=1}^{N_1} \sum_{j=1}^{N_2} (l_{i,j}^0 - l_{i,j}^1)^2}{N_1 N_2}} \\ w_r &= \sqrt{\frac{\sum_{i=1}^{N_1} \sum_{j=1}^{N_2} (r_{i,j}^0 - r_{i,j}^1)^2}{N_1 N_2}} \quad (18) \\ w_t &= \sqrt{w_l^2 + w_r^2} \end{aligned}$$

where l^0 and r^0 are the longitudinal trajectory and the radial trajectory manually drawn by the experts, l^1 and r^1 are the longitudinal trajectory and the radial trajectory computed by our approach, N_1 is the number of selected blocks and N_2

TABLE II
COMPARISON OF THREE BLOCK MATCHING CRITERIONS MAD, MSE AND NCC. THE SIGNIFICANCE TESTS REVEAL THAT THE TRACKING ERRORS (MEASURED BY w_l , w_r AND w_t IN MILLIMETERS) OF OUR APPROACH USING NCC HAVE SIGNIFICANT DIFFERENCE FROM THAT USING MAD AND MSE (THE SIGNIFICANCE LEVEL IS 0.05).

Method	w_l	w_r	w_t	
MAD	0.2946 (± 0.2199)	0.1466 (± 0.0488)	0.3391 (± 0.2013)	
MSE	0.2940 (± 0.2323)	0.1462 (± 0.0469)	0.3392 (± 0.2210)	
NCC	0.1933 (± 0.0807)	0.1156 (± 0.0370)	0.2293 (± 0.0759)	
P-value		w_l	w_r	w_t
NCC vs MAD		<0.01	<0.01	<0.01
NCC vs MSE		<0.01	<0.01	<0.01

is the number of images of each sequence. Then, different levels (1dB~30dB signal-noise ratio) of Rayleigh noise and Gaussian noise were artificially added to the ultrasound dataset in this study, and our approach was tested in this noise-corrupted dataset.

Finally, our approach was compared with three state-of-the-art methods (conventional block matching method (CBM) [7], Kalman-based block matching method (KBM) [11] and optical flow method (OP) [15], [25]). These methods were re-implemented by Matlab R2012a on a desktop computer with Intel(R) Xeon(R) CPU E5-2650 (2 GHz) and 32GB DDR2 memory. The sizes of the blocks and search regions in the four methods are identical, and other parameters used in these previous methods are identical with those provided in their publications.

C. Parameter Initialization

In order to select the optimum unscented transformation for our approach, our approach was tested using the unscented transformation UT_{2n} , scaled unscented transformation UT_{scal} , and symmetric unscented transformation UT_{sym} in Section II-C. It is necessary to determine three parameters in the UKF process in advance: the coefficient of the system noise variance q , coefficient of the observation noise variance r , and initial estimate variance \mathbf{P}_0 . In order to determine the appropriate values of the three parameters, the performance alteration of our approach when changing the three parameters was investigated. In order to select the optimum block-matching criterion for our approach, three commonly used block-matching criterions were compared, mean absolute difference (MAD), mean square error (MSE), and normalized cross correlation (NCC) (defined by [5]). Finally, the sizes of all the three reference blocks were set to be 0.5 mm \times 1.7 mm, and the sizes of the three search regions to be 1.3 mm \times 2.5 mm, where the center locations of the three search regions were same as those of the corresponding reference blocks.

IV. RESULTS

Figure 2(a)-(c) displays the performance of our approach when using q and r with the range (0,10] in three levels of \mathbf{P}_0 (0.1, 1 and 10). In each level of \mathbf{P}_0 , the smallest error of w_t was determined in the performance surface (marked by the red downward-pointing triangles). After comparing the three minimum values, it was determined that $r = 3$ and

TABLE III

RESULTS OF THE LINEAR MIXED-EFFECTS MODEL. "FULL MODEL" IS FORMULATED IN EQUATION (17). HYPOTHESIS TESTS ARE PERFORMED WITH THE NULL HYPOTHESIS THAT THE ESTIMATES EQUAL ZERO (THE SIGNIFICANCE LEVEL IS 0.05). THE PERCENTAGES ON THE RIGHT OF u_0 OR u_1 REVEAL THAT RATIO OF THE NUMBER OF SUBJECTS WITH STATISTICALLY SIGNIFICANT u_0 OR u_1 AMONG ALL THE SUBJECTS.

	LP				RP			
	Parameter	Estimate	Standard error	P-value	Parameter	Estimate	Standard error	P-value
Empty model	β_0	21.4554	0.2683	<0.01	β_0	21.4554	0.2683	<0.01
Full model	β_0	0.1784	0.0976	0.072	β_0	0.1468	0.8035	0.8566
	β_1	0.9920	0.0036	<0.01	β_1	0.9958	0.0394	<0.01
	β_2	0.0599	0.0492	0.2242	β_2	0.6799	0.4076	0.0953
	β_3	-0.0501	0.0613	0.4140	β_3	0.0873	0.5057	0.8629
	β_4	-0.0206	0.0281	0.4639	β_4	-0.1873	0.2310	0.4175
	β_5	-0.0024	0.0018	0.1809	β_5	-0.0349	0.0200	0.0811
	β_6	0.0023	0.0022	0.3093	β_6	-0.0059	0.0248	0.8111
	β_7	0.0009	0.0010	0.3979	β_7	0.0097	0.0113	0.3901
	u_0 (47.9%)	0.053 ± 0.4247	0.0657 ± 0.0106	<0.05	u_0 (46.0%)	-0.4275 ± 0.3131	0.5316 ± 0.0811	<0.05
u_1 (43.8%)	-0.0028 ± 0.0165	0.0027 ± 0.0004	<0.05	u_1 (46.0%)	0.0098 ± 0.1402	0.0258 ± 0.0037	<0.05	

$q = 5$ are optimal when the level of P_0 is 1. The values of r and q are fixed to be optimal, and the influence of the parameter P_0 on the performance of our approach was investigated. Figure 2(d) illustrates that the performance is optimum when $P_0 = 1$. Its variations in p-values when compared to $P_0 = 0, 2 - 12$ are all smaller than 0.01. This indicates that the error variation between optimal value (=1) and other values of P_0 in our approach are statistically significant. Table I presents the tracking error of our approach using the three unscented transformations. The results show that our approach exhibits the smallest error when using UT_{2n} rather than UT_{scal} and UT_{sym} with statistical significance. Table II shows the tracking errors of our approach using the three block matching criteria. The results indicate that our approach exhibits the optimum performance when using the NCC rather than MAD and MSE with statistical significance.

Table III shows the results of the linear mixed-effects model. The statistical significance of u_0 in the empty model indicates that the average magnitude of CCA wall motion varies significantly across subjects, and thus it is necessary to use the two-level model to interpret the dependence between our approach and the manual trace method. In terms of the fixed effects in equation (17), the estimate of β_0 and $\beta_2 \sim \beta_7$ are statistically insignificant either for LP or RP. This demonstrates that the health condition, sex, age, and their interactions with the results computed by our approach do not have fixed effect on the linear mixed-effects model. Therefore, it can be concluded that the correlation between our approach and manual traced method is not influenced by health condition, sex, and age of the subject. As regards the random effects, u_0 and u_1 in 47.9% and 43.8%, respectively, of the subjects are statistically significant when considering LP, and in 46.0% and 46.0%, respectively, of the subjects when considering RP. Although the statistical significance indicates that the correlation between our approach and manual traced method is influenced by these subjects, the degree of influence is negligible because the estimates of the significant u_0 and u_1 are close to zero (LP: $u_0 = -0.0530 \pm 0.4247$, $u_1 = -0.0028 \pm 0.0165$; RP: $u_0 = -0.4275 \pm 0.3131$, $u_1 = 0.0098 \pm 0.0075$).

Table IV shows the values of ICC in our approach and manual traced method (LP: $ICC(A,1)=0.9949$ and $ICC(C,1)=0.9957$; RP: $ICC(A,1)=0.9996$ and $ICC(C,1)=0.9996$).

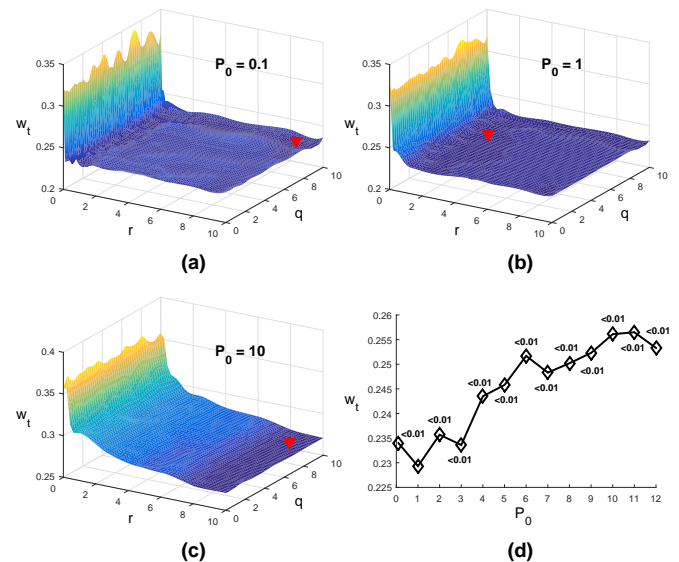


Fig. 2. The influence of the coefficients q and r of the noise on the performance of the proposed approach (measured by w_t) in three unequal orders of magnitude of the initial covariance P_0 of the state in the state-space equations: (a) $P_0 = 0.1$, (b) $P_0 = 1$, (c) $P_0 = 10$. The smallest values of w_t in various levels of P_0 are marked by the red downward-pointing triangles. By comparing the three smallest values of w_t , it can be determined that the proposed approach is optimum in (b), and the corresponding values of q and r are 5 and 3, respectively. (d) illustrates the influence of P_0 on the performance of our approach (measured by w_t) when $q = 5$ and $r = 3$. It can be seen that the performance is optimum (the smallest value of w_t) when $P_0 = 1$ with statistical significance compared to other values of P_0 .

Figure 3 shows the Bland-Altman plots between our approach and manual traced method. The average bias between the two methods is 0.0205 mm with confidence interval [-0.4640 mm, 0.4230 mm] for LP, and 0.0675 mm with confidence interval [-0.2755 mm, 0.1405 mm] for RP. Then, the scatter points were linearly fitted in the Bland-Altman plots. The slopes of the fitting lines (the blue lines in Figure 3) are 0.0076 for LP and 0.0028 for RP. This implies that their averages have little influence on difference between our approach and manual traced method. The results of ICC and Bland-Altman plots indicate that our approach exhibits reasonable agreement with the manual traced method.

Figure 4 displays the performance of our approach against

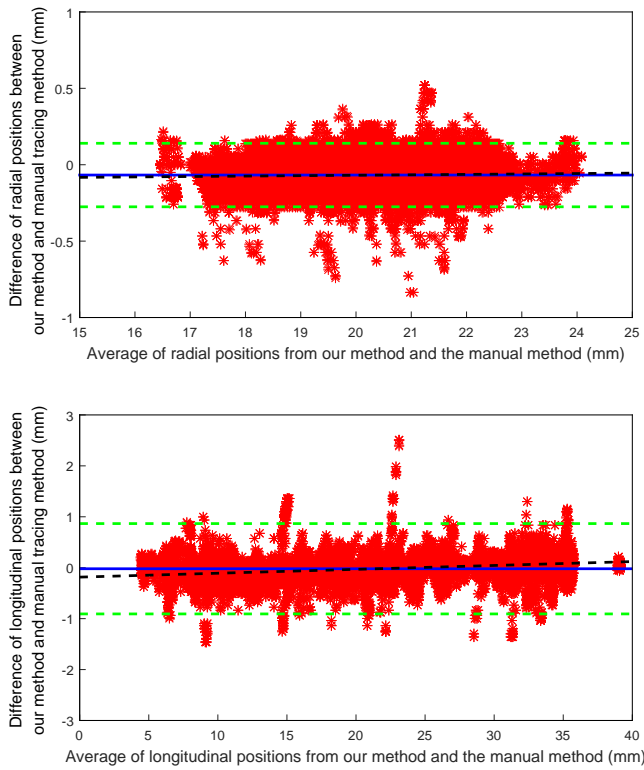


Fig. 3. Bland-Altman plots between our approach and manual tracing method with respect to the radial position (top) and longitudinal position (down) of the target block. The blue line represents the mean difference between our approach and the manual tracing method. The upper and lower green dashed lines show the 95% confidence interval of the mean difference (mean \pm 1.96 std). The black dashed line is the linearly fitting line of the scatter points in the plot.

the noise with various signal-noise ratios. The values of w_t increase by 0.1791 mm and 0.1578 mm with respect to 1dB Gaussian noise and Rayleigh noise, respectively. This can be an indication of the robustness of our approach to noise corruption in the tracking of CCA wall motion.

Table V presents the comparative results between our approach and previous methods. The results show that our approach has significantly smaller tracking error than the other methods, relative to the results acquired by the two observers (For Observer 1, w_l : 0.1922 ± 0.0799 mm, w_r : 0.1155 ± 0.0362 mm, w_t : 0.2282 ± 0.0751 mm; For Observer 2, w_l : 0.1944 ± 0.0828 mm, w_r : 0.1157 ± 0.0365 mm, w_t : 0.2301 ± 0.0782 mm). Moreover, the tracking error of our approach exhibits similar degree of variability as the intra-observer variability. In terms of computational efficiency, the computational cost of our approach was compared with those of the other methods. The results show that our approach (0.0257 ± 0.0046 second/frame) was moderately efficient compared to the other methods (CBM: 0.0249 ± 0.0049 second/frame; KBM: 0.0772 ± 0.0048 second/frame; OP: 0.0101 ± 0.0011 second/frame). Table VI shows that tracking errors of our approach have no significant difference on the subjects within different groups.

Table VII shows that our approach performs similarly on the synthetic image data with various central frequencies, and is

TABLE IV
INTRACLASS CORRELATION COEFFICIENTS (ICC) OF OUR APPROACH AND MANUAL TRACED METHOD. (C,1) IS THE ICC USING A CONSISTENCY DEFINITION AND (A,1) IS THE ICC USING AN ABSOLUTE AGREEMENT DEFINITION. A HYPOTHESIS TEST IS PERFORMED WITH THE NULL HYPOTHESIS THAT THE VALUE OF ICC EQUALS ZERO (THE SIGNIFICANCE LEVEL IS 0.05).

	ICC Type	ICC Value	Confidence Interval	P-value
LP	(C,1)	0.99575	[0.99561,0.99589]	<0.01
	(A,1)	0.99488	[0.99125,0.99665]	<0.01
RP	(C,1)	0.99966	[0.99964,0.99967]	<0.01
	(A,1)	0.99966	[0.99964,0.99967]	<0.01

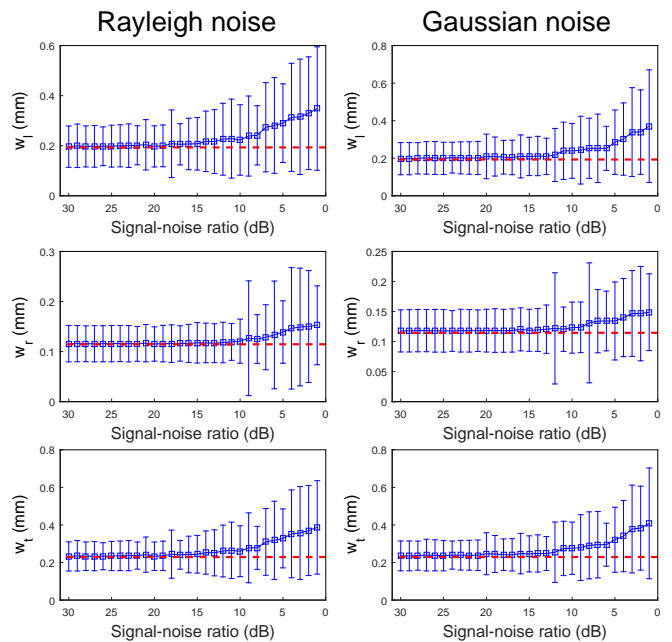


Fig. 4. Evaluation of the resistance of our approach to noise. Rayleigh noise (left column) and Gaussian noise (right column) with signal-to-noise ratio from 1 dB to 30 dB are artificially added to the dataset used in this study. The performance of our approach (measured by w_l , w_r and w_t) retested on the noise-corrupted dataset have shown as blue error bars. The red dashed lines display this performance on the original dataset without artificially adding the noise.

corrupted by Rayleigh noise and Gaussian noise. For the two types of noise, the increase of tracking error of our approach is smaller than 0.024 mm when the SNR equals 2dB. Moreover, the average tracking error of our approach is smaller than 0.15 mm. These results indicates the accuracy and robustness of our approach on the synthetic image data.

By the Mann-Whitney U test, Figure 5 illustrates that the difference of the peak-to-peak magnitudes of the radial and longitudinal CCA wall motions computed by our approach between healthy subjects and patients are statistically significant.

V. DISCUSSION

In this section, the experimental issues and performance of our approach as well as the clinical context of CCA wall motion are discussed.

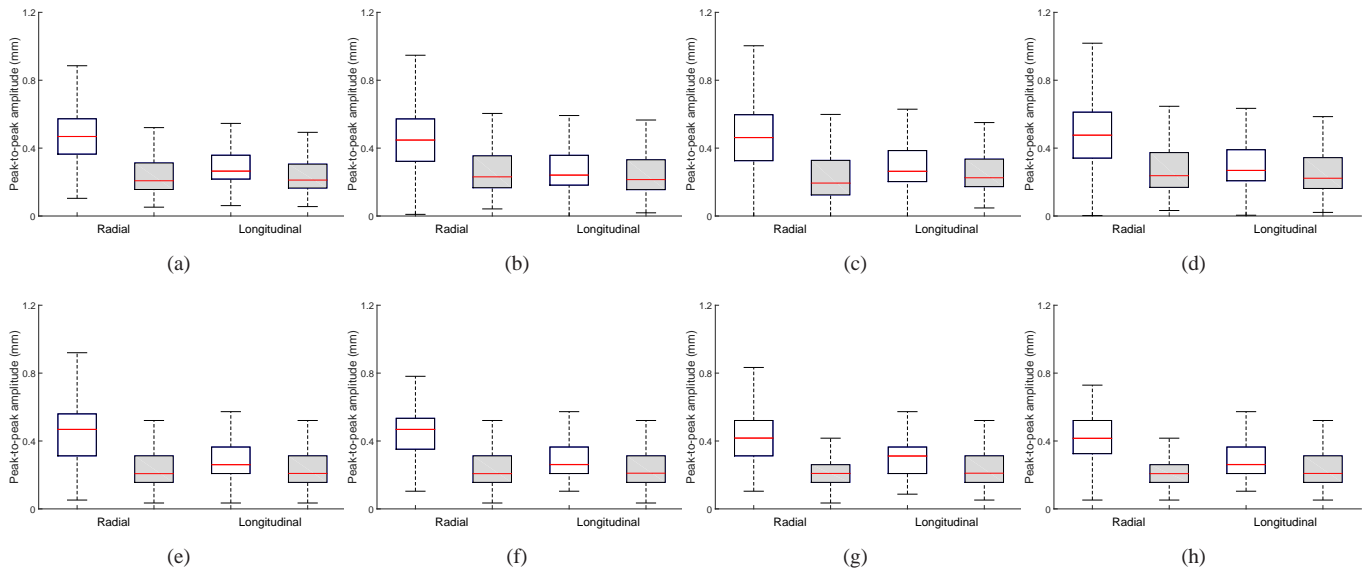


Fig. 5. The radial and longitudinal motion amplitudes for healthy subjects (white boxes) and patients (gray boxes) computed by (a) our approach, (b) KBM, (c) CBM, (d) OP, (e) MAD, (f) MSE, (g) UT_{scal} , and (h) UT_{sym} . For the radial and longitudinal motion amplitudes, Mann-Whitney U test shows that the p-values in (a)-(h) are all smaller than 0.01.

A. Model choice

The model selection is based on the assumptions about the motion of the CCA wall. From the viewpoint of the physiological aspects of CCA wall motion, this motion is affected by the dynamics of the blood pressure originating from the cardiac impulse. Thus, it can be assumed that the motion trajectory of the CCA wall is periodic or quasi-periodic, which has been experimentally validated by many previous studies [4], [7]. According to this assumption, a reasonable motion model of the CCA wall is to be periodic or quasi-periodic and moreover constrained by a motion model describing heart movement. Consequently, the state function f were generated in the proposed state-space approach motivated by the Van der Pol oscillator [13], which satisfies the quasi-periodic property and has been widely used in the description of the heart action [26], [27]. In addition, the control signal u_n was motivated by a mathematical model of the mechanical deformation of the CCA wall. This model was originated from a model of the intact left ventricle contraction [28] and has been validated on real clinical data [14], [15].

It is worth noting that our simplified model of the CCA wall motion according to the above assumption is not likely to completely match the real CCA wall motion because this motion may present various patterns in subjects with varying conditions such as periodontal disease [29]. From the perspective of the state-space theory, the component of the model mismatch can be considered as a part of the model uncertainty, which has been included in system noise w_n in Equation (1). This model uncertainty may affect the results of the state estimation and produce a negative effect on the performance of our approach. Thus, the model mismatch problem can be considered as the problem of accurately estimating the state value (i.e., location of the target tissue on the CCA wall in each ultrasound frame) by noise disturbance. In order to address this problem, UKF was applied to solve the state-space

TABLE V

COMPARISON WITH THREE STATE-OF-THE-ART METHODS (CBM, KBM AND OP), WITH RESPECT TO THE MANUAL TRACING RESULTS PERFORMED BY TWO EXPERIENCED ULTRASOUND PHYSICIANS. THE PERFORMANCE OF ALL THE TRACKING METHODS ARE MEASURED BY MEAN (\pm STANDARD DEVIATION) OF THE ERRORS w_l , w_r AND w_t IN MILLIMETERS. THE SIGNIFICANCE TESTS REVEAL THAT THE TRACKING ERRORS OF OUR APPROACH HAVE SIGNIFICANT DIFFERENCE WITH THE PREVIOUS METHODS (THE SIGNIFICANCE LEVEL IS 0.05).

Method	w_l	w_r	w_t
CBM vs observer 1	0.2867(0.2343)	0.1529(0.1919)	0.3334(0.2934)
CBM vs observer 2	0.2898(0.2284)	0.1587(0.1864)	0.3354(0.2853)
KBM vs observer 1	0.2332(0.1594)	0.1283(0.0860)	0.2703(0.1748)
KBM vs observer 2	0.2366(0.1565)	0.1319(0.0973)	0.2764(0.1767)
OP vs observer 1	0.2830(0.1321)	0.1217(0.0536)	0.3124(0.1327)
OP vs observer 2	0.2854(0.1329)	0.1261(0.0586)	0.3185(0.1359)
Our vs observer 1	0.1922(0.0799)	0.1155(0.0362)	0.2282(0.0751)
Our vs observer 2	0.1944(0.0828)	0.1157(0.0365)	0.2301(0.0782)
Inter-observer	0.1617(0.0709)	0.1080(0.0328)	0.1776(0.0742)
P-value	w_l	w_r	w_t
Our vs CBM	<0.01	<0.01	<0.01
Our vs KBM	<0.01	<0.01	<0.01
Our vs OP	<0.01	<0.01	<0.01

equations, which can reduce the noise disturbance under the minimum-mean-square-error criterion, i.e., reduce the negative effect of the model mismatch. Therefore, our approach can accommodate a range of time-varying CCA wall motion.

B. Experiment issues

Performance evaluation methods. The correlation was analyzed using the linear model. Although the simplicity and generalization of the linear model promotes its wide application, it is not capable of effectively analyzing data nested within various groups or embedded in various contexts [22]. In order to measure the potential influence from subjects with varied health conditions, sexes and ages, a two-level model was used to describe the motion tracking results, and the linear mixed-

TABLE VI

RESULTS OF THE TRACKING ERRORS BETWEEN OUR APPROACH AND MANUAL TRACING METHOD ON POPULATIONS WITH VARIED HEALTH CONDITIONS (HEALTHY/UNHEALTHY), SEXES (MALE/FEMALE), AND AGES (40~49, 50~59, 60~69, 70~79), AND ON ALL SUBJECTS. THE ERRORS ARE MEASURED BY MEAN (\pm STANDARD DEVIATION) OF THE ERRORS w_l , w_r AND w_t IN MILLIMETERS. THE DIGITS INSIDE THE BRACKETS DENOTE THE NUMBER OF SUBJECTS IN THE POPULATION. THE SIGNIFICANCE TESTS REVEAL THAT THE TRACKING ERRORS ON THE POPULATIONS WITH VARIED HEALTH CONDITIONS, VARIED SEXES, AND VARIED AGES HAVE NO SIGNIFICANT DIFFERENCE (THE SIGNIFICANCE LEVEL IS 0.05).

	w_l	w_r	w_t
All(103)	0.1933(0.0807)	0.1156(0.0370)	0.2293(0.0759)
Healthy(22)	0.1785(0.0667)	0.1195(0.0334)	0.2192(0.0596)
Unhealthy(81)	0.1945(0.0832)	0.1115(0.0379)	0.2286(0.0798)
Male(64)	0.1861(0.0724)	0.1127(0.0383)	0.2219(0.0685)
Female(39)	0.2023(0.0905)	0.1174(0.0320)	0.2385(0.0830)
40~49(27)	0.1833(0.0562)	0.1141(0.0347)	0.2190(0.0545)
50~59(32)	0.1760(0.0649)	0.1041(0.0322)	0.2087(0.0584)
60~69(20)	0.1843(0.0840)	0.1210(0.0289)	0.2255(0.0745)
70~79(24)	0.2282(0.0967)	0.1142(0.0402)	0.2602(0.0909)
P-value			
Health condition	0.1214	0.3363	0.8311
Sex	0.2409	0.4525	0.2464
Age	>0.3228	>0.1018	>0.0920

effects model was applied to analyze it (details are provided in Section III-B). Without considering the influence of various subject groups, the fixed effect β_0 and β_1 can be used to measure the degree of correlation from the viewpoint of model fitting. The value of β_0 (ideal value is 0) represents the average variation between the computed-aided method and manual traced method, and the value of β_1 (ideal value is 1) represents the degree of influence of the explanatory variable on the dependent variable. Moreover, the correlation can be divided into interclass correlation (Pearson's correlation coefficient) and intraclass correlation. The difference between the interclass correlation and intraclass correlation is that the former is suitable for analyzing the variables in various classes, and the latter is suitable for analyzing the variables in a common class. For the tracking results from the computer-aided method and manual traced method, the two types of tracking results can be considered as two observations of the CCA wall motion, and thus are variables in a common class. Therefore, the intraclass correlation is more suitable to measure the correlation. The intraclass correlation can be also considered to be an index to measure the agreement between the two methods, i.e., the extent to which the computer-aided method can replace the manual traced method. Owing to the variety of schemes to calculate the value of intraclass correlation, the Bland-Altman plot was used in order to intuitively display the agreement between the two methods.

Parameter initialization. The parameter initialization is crucial in the experiments as it determines the final values of the parameters used in the tracking method. A common method used to determine the parameter is to sample varied configurations of parameters and select the configuration corresponding to the minimum tracking error. These varied configurations of parameters are usually selected using two approaches. One of these approaches determines a subset of the domain of each parameter through user experience and extract the maximum

TABLE VII

RESULTS OF OUR APPROACH SEPARATELY PERFORMED ON 5MHZ, 7.5MHZ AND 10MHZ SYNTHETIC IMAGE DATA. THE TRACKING ERRORS ARE MEASURED BY w_t IN MILLIMETERS. THE COLUMNS "R" AND "G" DENOTE THE SYNTHETIC IMAGE DATA ARTIFICIALLY CORRUPTED BY RAYLEIGH NOISE AND GAUSSIAN NOISE WITH VARIOUS LEVELS OF SIGNAL-TO-NOISE RATIO. THE ROW " ∞ " DENOTES THE SYNTHETIC IMAGE DATA WITHOUT ARTIFICIALLY ADDED NOISE.

SNR	5MHz		7.5MHz		10MHz	
	R	G	R	G	R	G
∞	0.1260		0.1156		0.1161	
30	0.1270	0.1291	0.1156	0.1156	0.1161	0.1161
20	0.1307	0.1313	0.1167	0.1161	0.1167	0.1167
10	0.1338	0.1354	0.1229	0.1208	0.1172	0.1182
2	0.1500	0.1453	0.1296	0.1396	0.1271	0.1266

feasible number of parameter configurations from this subset. The other one considers the values of the parameters used in the previous studies as the initial parameter configurations. Verifying the parameter configuration corresponding to the minimum tracking errors is meaningful in statistics; the statistically significant configuration is to be tested to determine whether the minimum tracking error varies with other levels of tracking errors. Using the above scheme of parameter initialization, the values of the parameters q , r and \mathbf{P}_0 , the type of unscented transformation and the block-matching criterion were determined. These results are illustrated in Figure 2, Table I and Table II.

C. Performance

Our approach was compared with three state-of-the-art methods (CBM, KBM and OP). CBM is a model-free method because the block updating process in successive frames does not consider any correction of the motion trajectory from the predefined model. The stability of the CBM is easily violated by the varied image noise during the tracking process. The design of our approach has increased the resistance of the motion tracking process to the noise disturbance. The noise mainly originates from the instability of the local image structures from tissue homogeneity, low resolution of ultrasound imaging, out-of-plane motion, and tissue deformation during the movement of the CCA wall. In order to reduce the influence of this disturbance, a forward estimation model with Markovianity was applied such that the dynamics of the CCA wall also considers the information of the earlier CCA wall motion. This enables the motion process to prevent the block (which delimits the target tissue) from exhibiting significant displacement in the successive frames as this type of displacement is likely to imply that the block has lost its target. As a model-based method, KBM uses the forward model with Markovianity, and OP assumes that the brightness of the target is consistent during the movement. These constraints can enable the reduction of the disturbance from the noise. In contrast to KBM, a nonlinear quasi-periodic function expressed in equation (2) was proposed, to address the nonlinear components of the CCA wall motion, rather than use the conventional model that only considers the linear components of this motion. A mathematic model [14], [15] was also used, which describes the CCA wall motion as a time-variant control signal to substitute the constant control signal

in the same ultrasound sequence as that used in the previous methods. This improvement can facilitate the reduction of the cumulative bias of the motion trajectory during the tracking process. Furthermore, the UKF was adopted to obtain the optimal estimate of the target block. This does not require the computation of the Jacobian matrix and yields higher performance on the approximation of the non-linear function [17]. OP is another common motion tracking method, independent of the BM method, used to track CCA wall motion by producing the optical flow field in the successive frames. Table V shows the results of comparison with other methods. The tracking errors of the previous methods provided in IV is likely to vary from those presented in the publications. The varied tracking errors is caused by the non-uniformed image resolution and varied settings of ultrasound image (central frequencies, focusing range, field of view, etc.) in previous attempts. Another reason is that the testing data is not uniform because of varying experimental protocols and varying groups of subjects.

D. Clinical context

The investigations on atherosclerotic disease using the motion of the artery wall can be traced back to the last century. In the early stages, the radial motion has been extensively studied [30], [31] as it provided useful information for physiological research, such as those on vasoconstriction and vasodilation [32], arterial blood pressure [33], and many diseases such as hyperparathyroidism [34] and hyperlipidemia [35]. However, few studies paid attention to the longitudinal motion during this period because of the limitation of the vascular imaging technology, which hampered the detection of the longitudinal motion. In recent years, the multi-layer structure of the arterial wall and longitudinal motions can be clearly observed during cardiac cycle owing to the enhancements of ultrasound imaging technology [6]. Subsequent studies deemed that the longitudinal movement is no longer to be neglected because of the arterial dynamics as well as the availability of viable methods for extracting new information on arterial mechanical forces (such as wall shear stress) as a result of the increased knowledge of the longitudinal motion [36]. The significance of the longitudinal motion also has many physiological implications on the investigation of atherosclerotic disease. For instance, Svedlund et al. demonstrated that the longitudinal motion can predict short-term event-free survival in the subjects with medium-risk or high-risk coronary artery disease [37], and is also associated with the atherosclerotic plaque burden [38]. Ahlgren et al. showed that the administration of adrenaline can increase the amplitude of the longitudinal motion and enhance the intramural shear strain [39], [40]. These studies indicate to certain extent that the longitudinal motion can provide similar information as traditional risk markers [11]. Zahnd et al. carried out a series of critical studies to demonstrate that the longitudinal motion potentially provides extra and complementary information of arterial wall abnormalities in the early stage of coronary artery disease [4], [29].

VI. CONCLUSION

The dynamics of the CCA wall have been progressively considered to enable the stiffness evaluation of the carotid arteries. This can facilitate the early diagnosis of the atherosclerotic disease. In this study, we developed an approach to track the CCA wall motion by adopting the nonlinear state-space equations with a time-variant control signal based on a mathematical model of the carotid dynamics, which models the motion of the target tissue on the CCA wall. This approach was tested on the ultrasound sequences from a dataset of 103 subjects, and the experimental results demonstrate the effectiveness of this approach in the motion tracking of the CCA wall.

REFERENCES

- [1] S. J. Ziemann, V. Melenovsky, and D. A. Kass, "Mechanisms, pathophysiology, and therapy of arterial stiffness," *Arteriosclerosis, Thrombosis, and Vascular Biology*, vol. 25, no. 5, pp. 932–943, 2005.
- [2] L. M. van Bortel, T. de Backer, and P. Segers, "Standardization of arterial stiffness measurements make them ready for use in clinical practice," *American Journal of Hypertension*, vol. 29, no. 11, pp. 1234–1236, 2016.
- [3] M. Mokhtari-Dizaji, M. Montazeri, and H. Saberi, "Differentiation of mild and severe stenosis with motion estimation in ultrasound images," *Ultrasound in Medicine & Biology*, vol. 32, no. 10, pp. 1493–1498, 2006.
- [4] G. Zahnd, L. Boussel, A. Marion, M. Durand, P. Moulin, A. S erusclat, and D. Vray, "Measurement of two-dimensional movement parameters of the carotid artery wall for early detection of arteriosclerosis: a preliminary clinical study," *Ultrasound in Medicine & Biology*, vol. 37, no. 9, pp. 1421–1429, 2011.
- [5] A. Giachetti, "Matching techniques to compute image motion," *Image and Vision Computing*, vol. 18, no. 3, pp. 247–260, 2000.
- [6] M. Persson, A. R. Ahlgren, A. Eriksson, T. Jansson, H. W. Persson, and K. Lindstr om, "Non-invasive measurement of arterial longitudinal movement," in *IEEE International Ultrasonics Symposium*, vol. 2, 2002, pp. 1783–1786.
- [7] S. Golemati, A. Sassano, M. J. Lever, A. A. Bharath, S. Dhanjil, and A. N. Nicolaides, "Carotid artery wall motion estimated from B-mode ultrasound using region tracking and block matching," *Ultrasound in Medicine & Biology*, vol. 29, no. 3, pp. 387–399, 2003.
- [8] G. Zahnd, A. Marion, A. S erusclat, P. Moulin, L. Boussel, and D. Vray, "A new user-independent in vivo method for 2D motion estimation of the carotid wall by ultrasound imaging for early detection of pathological behavior," in *IEEE International Ultrasonics Symposium*, 2010, pp. 1348–1351.
- [9] A. Gastouniotti, S. Golemati, J. S. Stoitsis, and K. S. Nikita, "Kalman-filter-based block matching for arterial wall motion estimation from B-mode ultrasound," in *IEEE International Conference on Imaging Systems and Techniques (IST)*, 2010, pp. 234–239.
- [10] A. Gastouniotti, S. Golemati, J. S. Stoitsis, and K. S. Nikit, "Comparison of kalman-filter-based approaches for block matching in arterial wall motion analysis from B-mode ultrasound," *Measurement Science and Technology*, vol. 22, no. 11, 2011.
- [11] G. Zahnd, M. Orkisz, A. S erusclat, P. Moulin, and D. Vray, "Evaluation of a kalman-based block matching method to assess the bi-dimensional motion of the carotid artery wall in B-mode ultrasound sequences," *Medical Image Analysis*, vol. 17, no. 5, pp. 573–585, 2013.
- [12] A. Gastouniotti, S. Golemati, J. S. Stoitsis, and K. S. Nikita, "Carotid artery wall motion analysis from B-mode ultrasound using adaptive block matching: in silico evaluation and in vivo application," *Physics in Medicine and Biology*, vol. 58, no. 24, 2013.
- [13] R. Kandepu, B. Foss, and L. Imsland, "Applying the unscented kalman filter for nonlinear state estimation," *Journal of Process Control*, vol. 18, no. 7-8, pp. 753–768, 2008.
- [14] J. S. Stoitsis, S. Golemati, E. Bastouni, and K. S. Nikita, "A mathematical model of the mechanical deformation of the carotid artery wall and its application to clinical data," in *29th Annual International Conference of the IEEE Engineering in Medicine and Biology Society (EMBS)*, 2007, pp. 2163–2166.

- [15] S. Golemati, J. S. Stoitsis, A. Gastounioli, A. C. Dimopoulos, V. Koropouli, and K. S. Nikita, "Comparison of block matching and differential methods for motion analysis of the carotid artery wall from ultrasound images," *IEEE Transactions on Information Technology in Biomedicine*, vol. 16, no. 5, pp. 852–858, 2012.
- [16] E. A. Wan and R. van der Merve, "The unscented kalman filter for nonlinear estimation," in *IEEE Adaptive Systems for Signal Processing, Communications and Control Symposium*, 2000, pp. 153–158.
- [17] D. Simon, *Optimal State Estimation: Kalman, H_∞ and Nonlinear Approaches*. Wiley-Interscience, 2006.
- [18] D. J. Jwo, C. H. Tseng, J. C. Liu, and H. D. Lee, "Unscented kalman filtering for single camera based motion and shape estimation," *Sensors*, vol. 11, no. 8, pp. 7437–7454, 2011.
- [19] S. J. Julier and J. K. Uhlmann, "Consistent debiased method for converting between polar and cartesian coordinate systems," in *Proceeding of SPIE: Acquisition, Tracking and Pointing XI*, 1997.
- [20] S. Mendis, P. Puska, B. Norrving, S. Mendis, P. Puska, and B. Norrving, *Global Atlas on Cardiovascular disease prevention and control*. World Health Organization, 2011.
- [21] J. A. Jensen, "Field: A program for simulating ultrasound systems," in *10th Nordic-Baltic Conference on Biomedical Imaging*, 1996.
- [22] J. Wang, H. Xie, and J. H. Fisher, *Multilevel Models: Applications using SAS*. Higher Education Press, 2012.
- [23] K. O. McGraw and S. P. Wong, "Forming inferences about some intraclass correlation coefficients," *Psychological Methods*, vol. 1, no. 1, pp. 30–46.
- [24] J. M. Bland and G. D. Altman, "Statistical methods for assessing agreement between two methods of clinical measurement," *Lancet*, vol. 327, no. 8476, 1986.
- [25] B. K. Horn and B. G. Schunck, "Determining optical flow," *Artificial Intelligence*, vol. 17, no. 1-3, pp. 185–203.
- [26] B. Zduniak, M. Bodnar, and U. Forys, "A modified Van der Pol equation with delay in a description of the heart action," *International Journal of Applied Mathematics and Computer Science*, vol. 24, no. 4, pp. 853–863, 2014.
- [27] S. Das and K. Maharatna, "Fractional dynamical model for the generation of ECG like signals from filtered coupled van-der pol oscillators," *Computer Methods and Programs in Biomedicine*, vol. 112, no. 3, pp. 490–507, 2013.
- [28] M. Ledesma-Carbayo, J. Kybic, M. Desco, A. Santos, M. Suhling, P. Hunziker, and M. Unser, "Spatio-temporal nonrigid registration for ultrasound cardiac motion estimation," *IEEE Transactions on Medical Imaging*, vol. 24, no. 9, pp. 1113–1127, 2005.
- [29] G. Zahnd, D. Vray, A. Sérusclat, D. Alibay, M. Bartold, A. Brown, M. Durand, L. M. Jamieson, K. Kapellas, L. J. Maple-Brown, K. O'Dea, P. Moulin, D. S. Celermajer, and M. R. Skilton, "Longitudinal displacement of the carotid wall and cardiovascular risk factors: associations with aging, adiposity, blood pressure and periodontal disease independent of cross-sectional distensibility and intima-media thickness," *Ultrasound in Medicine & Biology*, vol. 38, no. 10, pp. 1705–1715, 2012.
- [30] R. W. Stadler, J. A. Taylor, and R. S. Lees, "Comparison of B-mode, M-mode and echo-tracking methods for measurement of the arterial distension waveform," *Ultrasound in Medicine & Biology*, vol. 3, no. 6, pp. 879–887, 1997.
- [31] Y. Zhang, N. Su, Z. Li, Z. Gou, Q. Chen, and Y. Zhang, "Assessment of arterial distension based on continuous wave doppler ultrasound with an improved Hilbert-Huang processing," *IEEE Transactions on Ultrasonics, Ferroelectrics, and Frequency Control*, vol. 57, no. 1, pp. 203–213, 2010.
- [32] S. Schwarzacher, F. Weidinger, K. Krejcy, and G. Raberger, "Assessment of changes in vasomotor tone in vivo using intravascular ultrasound," *Journal of Pharmacological and Toxicological Methods*, vol. 28, no. 3, pp. 143–147, 1992.
- [33] L. M. van Bortel, E. J. Balkestein, J. J. van der Heijden-Spek, F. H. Vanmolkot, J. A. Staessen, J. A. Kragten, J. W. Vredeveld, M. E. Safar, H. A. S. Boudier, and A. P. Hoeks, "Non-invasive assessment of local arterial pulse pressure: comparison of applanation tonometry and echo-tracking," *Journal of Hypertension*, vol. 19, no. 6, pp. 1037–1044, 2001.
- [34] L. A. Bortotolotto, V. Costa-Hong, V. Jorgetti, F. Consolim-Colombo, K. Rosa, B. C. Silva, E. M. Krieger, and J. J. D. Lima, "Vascular changes in chronicrenal disease patients with secondary hyperparathyroidism," *Journal of Nephrology*, vol. 20, no. 1, pp. 66–72, 2007.
- [35] T. Montalcini, G. Gorgone, C. Gazzaruso, and A. Pujia, "Carotid distension and distensibility impairment in individuals affected by familial combined hyperlipidemia," *Atherosclerosis*, vol. 212, no. 1, pp. 177–180, 2010.
- [36] M. Persson, A. R. Ahlgren, T. Jansson, A. Eriksson, H. W. Persson, and K. Lindström, "A new non-invasive ultrasonic method for simultaneous measurements of longitudinal and radial arterial wall movements: first in vivo trial," *Clinical Physiology and Functional Imaging*, vol. 23, no. 5, pp. 247–261, 2003.
- [37] S. Svedlund, C. Eklund, P. Robertsson, M. Lomsky, and L.-M. Gan, "Carotid artery longitudinal displacement predicts 1-year cardiovascular outcome in patients with suspected coronary artery disease," *Arteriosclerosis, Thrombosis, and Vascular Biology*, vol. 31, no. 7, pp. 1668–1674, 2011.
- [38] S. Svedlund and L. ming Gan, "Longitudinal common carotid artery wall motion is associated with plaque burden in man and mouse," *Atherosclerosis*, vol. 217, no. 1, pp. 120–124, 2011.
- [39] A. R. Ahlgren, M. Cinthio, S. Steen, H. W. Persson, T. Sjöberg, and K. Lindström, "Effects of adrenaline on longitudinal arterial wall movements and resulting intramural shear strain: a first report," *Clinical Physiology and Functional Imaging*, vol. 29, no. 5, pp. 353–359, 2009.
- [40] A. R. Ahlgren, M. Cinthio, S. Steen, T. Nilsson, T. Sjöberg, H. W. Persson, and K. Lindström, "Longitudinal displacement and intramural shear strain of the porcine carotid artery undergo profound changes in response to catecholamines," *American Journal of Physiology-Heart and Circulatory Physiology*, vol. 302, no. 5, pp. H1102–H1115, 2012.